Combined measurement of velocity and temperature in liquid metal convection

Zürner, T.; Schindler, F.; Vogt, T.; Eckert, S.; Schumacher, J.;

Originally published:

August 2019

Journal of Fluid Mechanics 876(2019), 1108-1128

DOI: https://doi.org/10.1017/jfm.2019.556

Combined measurement of velocity and temperature in liquid metal convection

Till Zürner[1]†, Felix Schindler[2], Tobias Vogt[2], Sven Eckert[2] and Jörg Schumacher[1]

[1]Institute of Thermodynamics and Fluid Mechanics, Technische Universität Ilmenau, Postfach 100565, D-98684 Ilmenau, Germany

[2]Department of Magnetohydrodynamics, Institute of Fluid Dynamics, Helmholtz-Zentrum Dresden-Rossendorf, Bautzner Landstraße 400, D-01328 Dresden, Germany

(Received xx; revised xx; accepted xx)

Combined measurements of velocity components and temperature in a turbulent Rayleigh-Bénard convection flow at a low Prandtl number of $Pr = 0.029$ and for Rayleigh numbers between $10^6 \leqslant Ra \leqslant 6 \times 10^7$ are conducted in a series of experiments with durations of more than a thousand free fall time units. Multiple crossing ultrasound beam lines and an array of thermocouples at mid-height allow for a detailed analysis and characterization of the complex three-dimensional dynamics of the single large-scale circulation (LSC) roll in the cylindrical convection cell of unit aspect ratio which is filled with the liquid metal alloy GaInSn. We extract the superposition of short-term oscillations of the LSC with different orientation angles close to the top/bottom plates and the related sloshing motion in the mid-plane with the slow azimuthal drift of the mean roll orientation as a whole that proceeds on a hundred times slower time scale, and measure the internal temporal correlations of this complex large-scale flow. The coherent LSC drives a vigorous turbulence in the whole cell that is quantified by direct Reynolds number measurements at different locations in the cell. The velocity increment statistics in the bulk of the cell displays characteristic properties of intermittent small-scale fluid turbulence. We also show that the impact of the symmetry-breaking large-scale flow persists to small-scale velocity fluctuations thus preventing the establishment of isotropic turbulence in the cell center. Reynolds number amplitudes depend sensitively on beam line position in the cell such that different definitions have to be compared. The global momentum and heat transfer scalings with Rayleigh number are found to agree with those of direct numerical simulations and other laboratory experiments.

1. Introduction

The understanding of transport processes in several turbulent convection flows in nature and technology can be improved by means of Rayleigh-Bénard convection (RBC) studies at very low Prandtl numbers of $Pr \ll 10^{-1}$. Prominent examples are stellar and solar convection (Spiegel 1962), the geodynamo in the core of the Earth (Christensen & Aubert 2006), the blanket design in nuclear fusion reactors (Salavy *et al.* 2007) or liquid metal batteries for renewable energy storage (Kelley & Weier 2018). Laboratory experiments in turbulent RBC at low Prandtl numbers are, however, notoriously challenging since they have to rely on liquid metals as working fluid to obtain a sufficiently high thermal diffusivity in comparison to the kinematic viscosity. Liquid metals are opaque

† Email address for correspondence: till.zuerner@tu-ilmenau.de

and thus exclude optical imaging by means of particle image velocimetry (Adrian & Westerweel 2011) or Lagrangian particle tracking (Hoyer *et al.* 2005; Toschi & Bodenschatz 2009). The analysis relies instead on ultrasound Doppler velocimetry (UDV, Takeda 1987) in combination with local temperature measurements. We mention here pioneering experiments by Takeshita *et al.* (1996); Cioni *et al.* (1997); Mashiko *et al.* (2004); Tsuji *et al.* (2005) and more recently by Khalilov *et al.* (2018), or Vogt *et al.* (2018*a*), who found a jump-rope-type large-scale flow.

In closed convection cells, a large-scale circulation (LSC) builds up that affects the way and amount of heat and momentum carried across the turbulent fluid (Ahlers *et al.* 2009; Chillà & Schumacher 2012). Its complex three-dimensional shape and dynamics have been studied intensively in the past decade for RBC flows with $Pr > 0.1$, for example in theoretical oscillator models (Brown & Ahlers 2009), experiments (Funfschilling & Ahlers 2004; Sun *et al.* 2005; Xi *et al.* 2009; Zhou *et al.* 2009), and direct numerical simulations (Stevens *et al.* 2011; Shi *et al.* 2012). The low-Prandtl number regime has been largely unexplored with respect to the large-scale flow dynamics. Only recently, the interest in this research topic has increased with new experiments by Khalilov *et al.* (2018) and Vogt *et al.* (2018*a*). The typical cylindrical cell shape leads to a statistical symmetry of convective turbulence with respect to the azimuthal direction and opens the possibility to complex LSC dynamics. These consist of shorter-term oscillations of the mean flow orientation close to the plates which point into different directions at top and bottom. The oscillations can be superimposed by a slow azimuthal drift of the mean flow orientation of the LSC roll as a whole. The UDV technique has been proved to detect complex flow structures in liquid metal thermal convection (Mashiko *et al.* 2004; Tsuji *et al.* 2005; Vogt *et al.* 2018*a*,*b*). This method has been extended recently to linear transducer arrays that allow to reconstruct 2D flow patterns at high spatial and temporal resolution (Franke *et al.* 2013).

In this work, we report first multi-technique long term measurements of a fully turbulent convection flow in the liquid metal alloy gallium-indium-tin (GaInSn, $Pr = 0.029$) in a closed cylindrical cell of aspect ratio 1. We combine eight UDV beam lines and 11 thermocouples for an in-depth analysis of the LSC at Rayleigh numbers $Ra \lesssim 10^8$. Multiple crossing UDV beam lines close to the bottom/top walls and at the mid-plane in combination with an array of thermocouple probes arranged in a semicircle of high angular resolution at half height enable the detailed experimental reconstruction of a short-term oscillatory torsional motion of the LSC at top and bottom, the sloshing motion at half height and the superposition of this short-term dynamics with a slow azimuthal drift. The LSC flow is found to be more coherent as in comparable RBC flows at higher Prandtl numbers agreeing also with recent direct numerical simulations (DNS) of Scheel & Schumacher (2016, 2017) in the same parameter range. Our analysis reveals a LSC roll with large inertia able to drive a vigorous fluid turbulence in the bulk, the latter of which is detected from direct determination of the Reynolds number dependence $Re(Ra)$ in the cell centre using UDV. On the basis of this measurement method, we will also analyse the statistics of velocity increments and the isotropy of small-scale turbulence in the liquid metal flow. Our experiment yields time series of velocity components and temperature of almost two thousand free-fall times units. Although three-dimensional high-resolution direct numerical simulations (DNS) of such flows provide the full information of the turbulent fields, they cannot be run for extended time intervals of a few hundred convective time units or even more (van der Poel *et al.* 2013; Scheel & Schumacher 2016, 2017). These experiments are thus the only way to conduct a long-term global analysis of three-dimensional LSC flow that has to be considered as a superposition of different modes with different typical time scales.

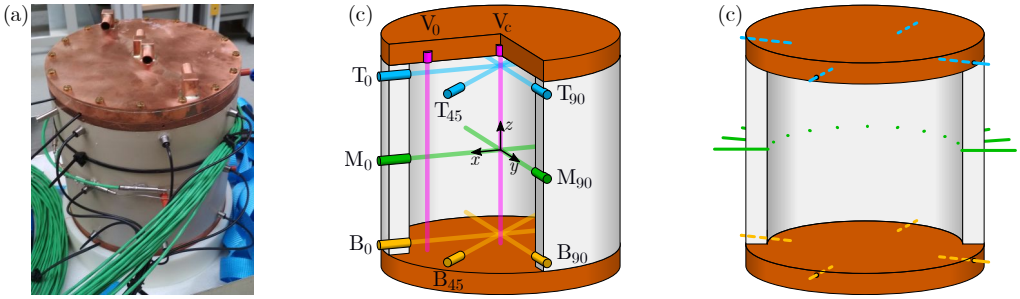

FIGURE 1. Convection cell design and arrangement of ultrasound beam lines and thermocouples. (a) Photograph. (b) Positions and labels of the ultrasound Doppler velocimetry sensors. The subscripts of the labels refer to the azimuthal position in degree. (c) Positions of the temperature sensors. The side-walls are thermally insulated during the experiment.

The outline of the manuscript is as follows. In section 2 we present details on the experiment. Section 3 is dedicated to the large-scale flow in the cell. We discuss the oscillation of the azimuthal orientation, torsion as well as the sloshing modes by means of three representative runs that cover the whole range of Rayleigh numbers. For one particular run, we study a cessation event in detail. Furthermore, we take in this section a closer look to the internal temporal correlations of the large-scale flow. Section 4 reviews the global transport of heat and momentum. Section 5 provides our findings for the statistics of the velocity increments. We close the work with a final summary and give a brief outlook into future work.

2. Experimental set-up

The cylindrical convection cell (figure 1(a)) has an inner diameter $D = 2R = 180\,\mathrm{mm}$ and an inner height $H = 180\,\mathrm{mm}$ with aspect ratio $\Gamma = D/H = 1$. The side walls are made of polyether ether ketone (PEEK), and the top and bottom plates consist of copper with a thickness of 25 mm. The top plate is cooled with water supplied by a thermostat. A ceramic heating plate with a diameter of 190 mm is mounted below the bottom copper plate, supplying a maximum heating power of 2 kW for DC voltage of 230 V. The cell is filled with the eutectic alloy gallium-indium-tin (GaInSn, melting point 10.5 °C). The mean temperature $\bar{T}$ in the experiments of about 35 °C gives a Prandtl number of $Pr = 0.029$. The properties of GaInSn are then: mass density $\rho = 6.3 \times 10^3\,\mathrm{kg/m^3}$, kinematic viscosity $\nu = 3.2 \times 10^{-7}\,\mathrm{m^2/s}$, thermal diffusivity $\kappa = 1.1 \times 10^{-5}\,\mathrm{m^2/s}$, thermal conductivity $\lambda = 24.3\,\mathrm{W/(K\,m)}$, and volumetric expansion coefficient $\alpha = 1.2 \times 10^{-4}\,1/\mathrm{K}$ (Müller & Bühler 2001; Plevachuk *et al.* 2014). The Rayleigh number varies between $10^6 \leqslant Ra \leqslant 6 \times 10^7$ thus covering almost two orders of magnitude.

The velocity measurements rely on the pulsed UDV technique applying a specific configuration (figure 1(b)), where eight transducers emit ultrasonic pulses with a frequency of 8 MHz along a straight beam line and record the echoes that are reflected by small particles in the fluid. Knowing the speed of sound in GaInSn allows us to determine the spatial particle position along the ultrasound propagation from the detected time delay between the burst emission and the echo reception. The movement of the scattering particles, which are always dispersed in a GaInSn melt, results in a small time shift of the signal structure between two successive bursts from which the velocity can be calculated.

The plate temperatures are measured as the average of four K-thermocouples distributed in 90° intervals around the plate circumference (blue and orange in figure 1(c)).

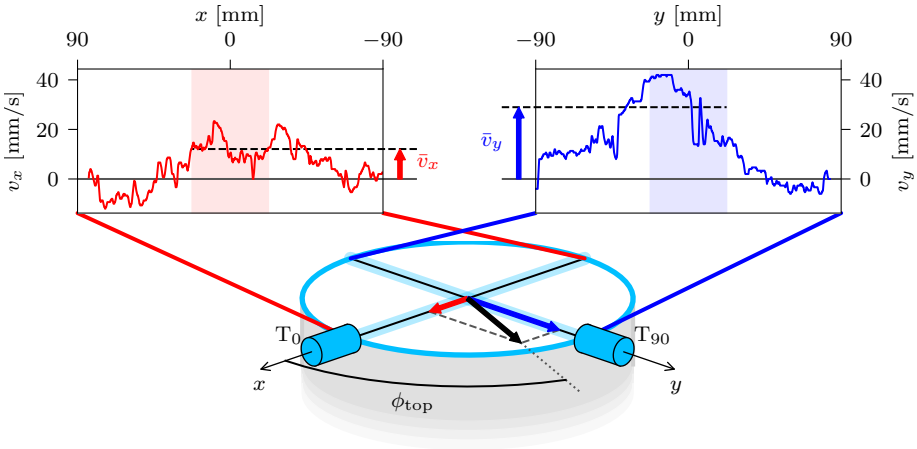

FIGURE 2. Calculation of the orientation angle ϕ_{top} of the large-scale flow close to the top plate. The UDV sensor T_0 at $\phi = 0°$ measures the radial v_x profile (red) and T_{90} at $\phi = 90°$ measures the radial v_y profile (blue). The mean velocities $\bar{v}_x$ and $\bar{v}_y$ are determined over the central shaded profile intervals. These values are used as components of the horizontal velocity vector of the LSC $\boldsymbol{v}_{\text{top}}$ (black arrow).

Eleven additional thermocouples are arranged at half height of the convection cell in a semicircle in steps of 18° (green in figure 1(c)).

The global heat flux $\dot{Q}$ is determined at the top plate: The inflowing cooling water of temperature T_{in} heats up to a temperature T_{out} at the outlet. In combination with the water volume flux $\dot{V}$ the extracted heat flux is $\dot{Q}_{\text{cool}} = \tilde{c}_p \tilde{\rho} \dot{V}(T_{\text{out}} - T_{\text{in}})$ with $\tilde{c}_p$ and $\tilde{\rho}$ being the isobaric heat capacity and mass density, respectively, of the cooling water. Measurements with $T_{\text{out}} - T_{\text{in}} > 0.2\,\text{K}$ are considered only. Heat losses through the side wall are determined by measuring the radial temperature gradient $\partial_r T$ in the side wall from three additional pairs of thermocouples at half height and azimuthal positions in 120° intervals. The radial heat flux is $\dot{Q}_{\text{loss}} = -\lambda_{\text{sidewall}} \pi D H \partial_r T$. Half of the average heat loss is then added to $\dot{Q}_{\text{cool}}$.

3. Large-scale flow dynamics

3.1. *Long-term dynamics of the large-scale flow structure*

We now discuss the long-time evolution of the LSC for a measurement at one of the highest Rayleigh numbers, $Ra = 6 \times 10^7$. Times are given in units of the free-fall time $\tau_{\text{ff}} = \sqrt{H/(g\alpha\Delta T)}$. Variable g is the acceleration due to gravity. For the example data set at $Ra = 6 \times 10^7$, the free fall time is $\tau_{\text{ff}} = 2.3\,\text{s}$ and the total duration of the time series is $1700\tau_{\text{ff}}$. Figure 2 illustrates how the orientation angle of the flow in the centre close to the top plate is calculated. The velocity profiles $v_x(x,t)|_{y=0}$ and $v_y(y,t)|_{x=0}$ are measured by UDV sensors T_0 and T_{90}, 10 mm below the top plate. At the central crossing point of the ultrasonic beams the horizontal velocity vector $\boldsymbol{v}_{\text{top}} = (\bar{v}_x, \bar{v}_y)$ and the resulting orientation angle are given by

$$\bar{v}_i(t) = \langle v_i(i,t) \rangle_{-D/8 \leqslant i \leqslant D/8}\,, \qquad \text{and thus} \qquad \phi_{\text{top}} = \arctan\left(\frac{\bar{v}_y}{\bar{v}_x}\right), \tag{3.1}$$

with $i = x, y$. The orientation angle at the bottom plate ϕ_{bot} is calculated analogously using UDV sensors B_0 and B_{90}. Figure 3(a) shows a time series of $\phi_{\text{top}} + 180°$ and ϕ_{bot}. The two angles match very well which implies that in this measurement they always

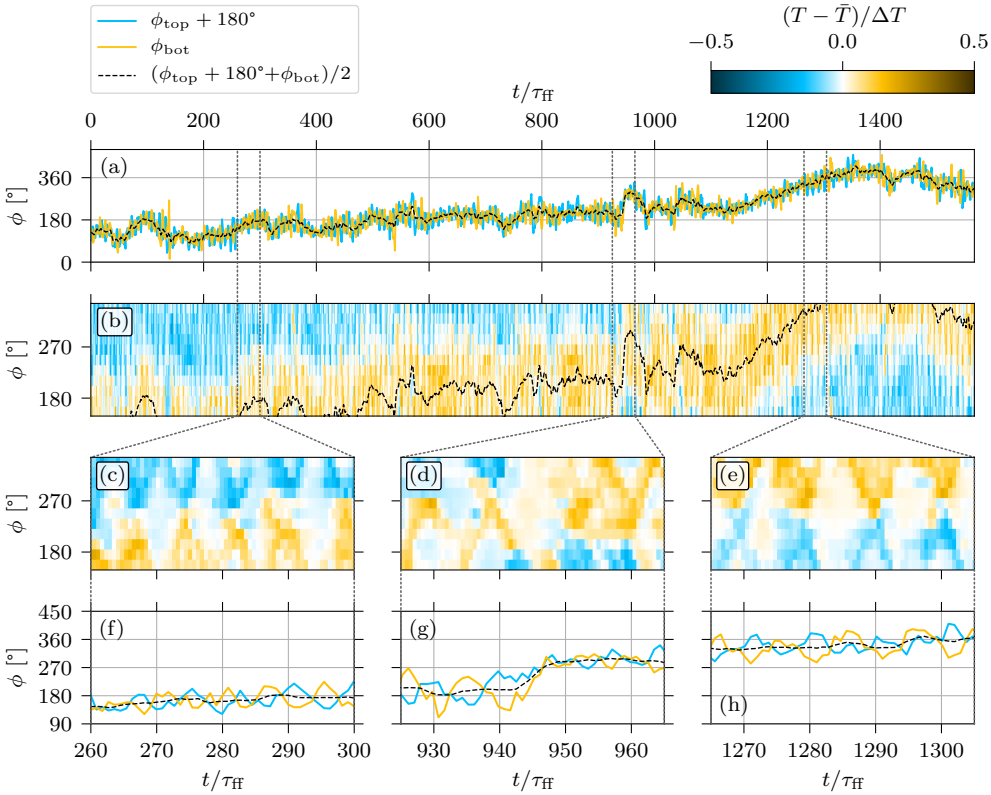

FIGURE 3. Large-scale flow for $Ra = 6 \times 10^7$ ($\tau_{\mathrm{ff}} = 2.3\,\mathrm{s}$). (a) LSC orientation angles at the top and bottom plate calculated from the UDV measurements (see figure 2). The black dashed line is the smoothed average of the top and bottom angles. (b) Temperatures near the wall at half height of the cell over time and azimuthal position. The dashed black line is identical to the one in panel (a). (c)–(e): Detailed views of time series (b) for a time interval of $40\tau_{\mathrm{ff}}$. (f)–(h): Detailed views of time series (a) for same time interval.

maintain a mean azimuthal offset of 180°. This validates the presence of a single coherent LSC roll in the cell. Figures 3(d) and (f) present a detailed view of the data in figure 3(a). It can now be seen that the orientation angles oscillate around a common mean at an oscillation time of $\tau_{\mathrm{osc}} \sim 10\tau_{\mathrm{ff}}$. Furthermore, the angles oscillate in anti-phase, which is a clear indication of the twisting mode. The LSC flow is thus characterized by a torsion in agreement with DNS at similar Pr by Scheel & Schumacher (2016, 2017) and experiments in liquid sodium (Khalilov *et al.* 2018, $Pr = 0.008$). We come back to this point in section 3.2. Panel (a) of this figure shows clearly the additional slow drift of the mean orientation angle by more than 180° over the full measurement time period of $\tau_{\mathrm{total}} \approx 1700\tau_{\mathrm{ff}}$, a motion that is due to the statistical azimuthal symmetry in the cylindrical setup. The characteristic time scale of this motion can be estimated to be of the order of $\tau_{\mathrm{drift}} \sim 10^3\tau_{\mathrm{ff}}$.

Most experiments on the large scale flow structure in turbulent RBC use temperature measurements close to the side walls of the cell to infer the azimuthal profile of the vertical flow direction from their temperature imprint: Up-welling fluid from the hot bottom plate is detected as a high temperature signal, while down-welling fluid from the cold top plate gives a low signal. This principle is employed here as well, however at a very fine resolution. Figure 3(b) shows a colour plot of the temperature time

series taken simultaneously by 11 thermocouples which are arranged in a semicircle at the side-wall at half height (see figure 1(c)). This arrangement allows us to present a space-time-plot of temperature with details never obtained before in a liquid metal flow experiment. Temperatures below the average fluid temperature $\bar{T}$ are coloured in blue and temperatures above $\bar{T}$ are shown in orange. The black dashed line re-plots a smoothed profile of the LSC orientation $\phi_{\mathrm{LSC}} = (\phi_{\mathrm{top}} + 180 + \phi_{\mathrm{bot}})/2$ from figure 3(a) and confirms the coherence of the average LSC: Temperature at half height and velocity dynamics at top/bottom are in perfect synchronization and drift slowly as a common, single LSC roll.

Figures 3(c) and (e) show magnified sections at finer temporal resolution that correspond to those in panels (d) and (f), respectively. In both cases, hot rising and cold falling plumes at the side-wall bounce together and move away of each other again. This periodic motion is known as a sloshing mode of the LSC (Zhou *et al.* 2009; Brown & Ahlers 2009). We detect $\tau_{\mathrm{slosh}} = \tau_{\mathrm{osc}}$ from these two pairs of panels. Previous experiments in water (Zhou *et al.* 2009; Brown & Ahlers 2009) report that the up- and down-welling flows come as close as 45°. In our measurements this minimal azimuthal distance is much smaller, regularly reaching the order of our azimuthal resolution of 18°. This extreme sloshing amplitude seems to be a property of low-Pr convection and the high inertia of liquid metals.

A rare event in the large-scale flow dynamics is shown in figure 3(d) and (g). Here, the LSC rapidly changes its orientation by about 90° within less than $10\tau_{\mathrm{ff}}$. At the same time, the characteristic sloshing pattern in the temperature plot is disrupted and over most of the circumference the mean value of the temperature is detected which is in line with the absence of the coherent pattern up- or down-welling flow. Only after the sudden orientation change the sloshing pattern reappears, now shifted by 90°in azimuthal direction. This observation suggests that a cessation has taken place, events which have also been observed in experiments with water (Brown & Ahlers 2006) and fluorinert FC-77 (Xie *et al.* 2013). Cessations consist of a breakdown of the coherent LSC into an incoherent flow state and a subsequent re-establishment of the coherence of the LSC with a different orientation. These events are rare; they occurred at rates of the order of days^{-1} (Brown & Ahlers 2006; Xie *et al.* 2013). Our time series cannot reach to such durations such that a statistical analysis of cessations in liquid metal convection was not possible.

In figure 4, two additional experiments – one at the lowest Rayleigh number $Ra = 10^6$ and one at an intermediate $Ra = 10^7$ – are presented. The time series cover again more than 1000 free-fall times in both cases. Just as for $Ra = 6 \times 10^7$ in figure 3, the temperature and velocity measurements show the presence of the a LSC, as well as sloshing and twisting modes in the magnifications. Differences can mainly be seen with respect to the temperature magnitude when comparing the data to figure 3. With increasing Ra, the amplitude of the fluid temperature at mid-height of the cell decreases steadily indicating an enhanced mixing of the scalar field due to an increasingly inertial fluid turbulence. Furthermore, the hot and cold patches of the up- and down-wellings are thicker and more washed out for lower Rayleigh numbers. This can be seen best for the lowest $Ra = 10^6$ in figure 4(d). We have found that the magnitude of the total long-term azimuthal drift does not show a dependence on the Rayleigh number in the accessible range. To summarize this part, our experimental study shows clearly that the LSC dynamics have to be considered as superposition of multiple processes with different characteristic time scales which can be reconstructed from the time series.

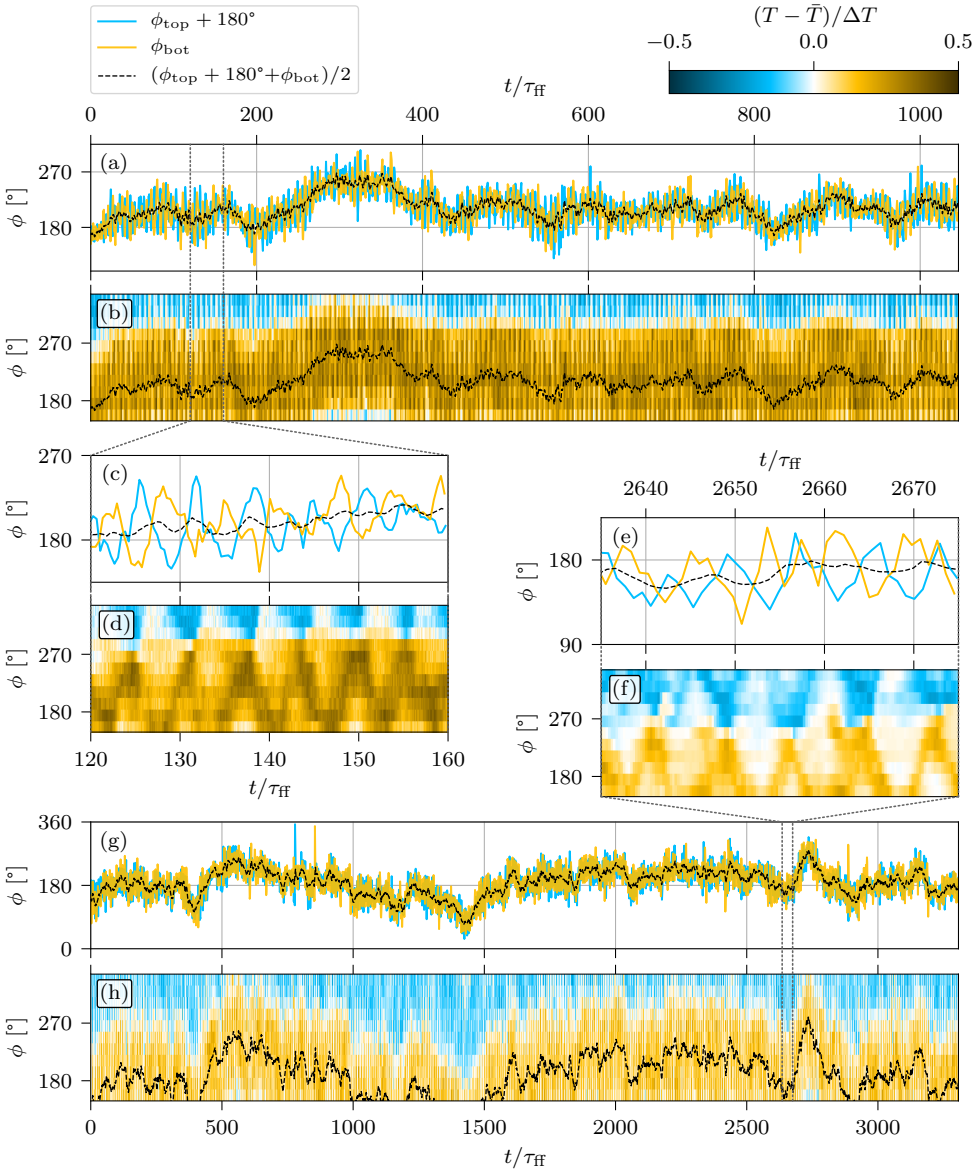

FIGURE 4. Large-scale flow for $Ra = 10^6$ ($\tau_{\mathrm{ff}} = 17\,\mathrm{s}$, (a–d)) and $Ra = 10^7$ ($\tau_{\mathrm{ff}} = 5.4\,\mathrm{s}$, (e–h)). The quantities and colour scales are the same as in figure 3. (c) and (d) are detailed views of (a) and (b), respectively. (e) and (f) are detailed views of (g) and (h), respectively. The timespan of the detailed views is $40\tau_{\mathrm{ff}}$. The color scale is the same as in figure 3.

3.2. *Rayleigh number dependence of oscillation frequencies*

Frequency spectra of ϕ_{top} are shown for three Rayleigh numbers Ra in figure 5(a). A clear peak gives the oscillation frequency f_{osc} of the torsional mode. The characteristic frequency value is extracted by a fit of a combination of an algebraic power law and a Gaussian distribution to the data. Figure 5(b) shows the Ra-dependence of the frequency f_{osc}, normalized by the thermal diffusion frequency

$$f_{\mathrm{td}} = \frac{\kappa}{H^2}\,. \tag{3.2}$$

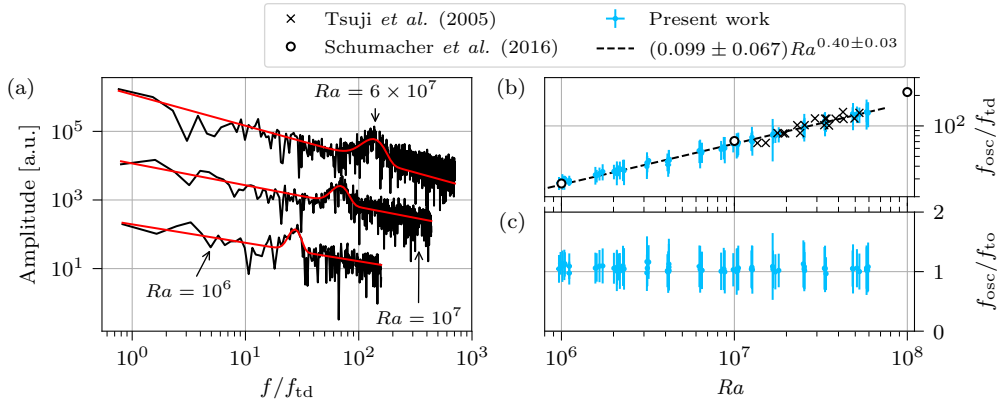

FIGURE 5. (a) Frequency spectra of ϕ_{top} for different Ra, normalized by the thermal diffusion frequency f_{td}. The spectra at $Ra = 10^6$ and $Ra = 6 \times 10^7$ are shifted for a better visibility by a factor of 0.1 and 20, respectively. The red lines are fits to the spectra to determine the characteristic oscillation frequency f_{osc}. (b) Scaling of the frequency f_{osc} with Ra. The error bars are taken from the standard deviation of the Gaussian fit. (c) Comparison of f_{osc} to the turnover frequency f_{to} over Ra.

The error bars correspond to the standard deviation of the fitted Gaussian distributions. A power law fit, which is indicated as a dashed line in figure 5(b), gives a scaling of $f_{\text{osc}}/f_{\text{td}} \simeq (0.10 \pm 0.04)Ra^{0.40\pm0.02}$. Dimensional arguments suggest a scaling of the oscillation frequency with the free-fall time τ_{ff} of $f_{\text{osc}} \propto Ra^{0.5}$ for constant material properties, since $1/\tau_{\text{ff}} = \sqrt{\nu\kappa Ra}/H^2$. The exponent of 0.4 indicates, that the underlying time-scale is indeed close to the free-fall time, but that the inertial character of the fluid turbulence in the low-Prandtl-number flow affects the turbulent momentum transfer. We will return to this point in section 4.2.

DNS by Schumacher *et al.* (2016) at $Pr = 0.021$ result in a slightly stronger scaling of $f_{\text{osc}}/f_{\text{td}} \simeq (0.08\pm0.05)Ra^{0.42\pm0.02}$ when their data are corrected from radians to units of cycles per diffusive time (open circles in figure 5(b)). Previous experiments by Tsuji *et al.* (2005) in mercury at a Prandtl number of $Pr = 0.024$ coincide with our results (crosses in figure 5(b)). For liquid gallium in a $\Gamma = 2$ cell ($Pr = 0.027$) Vogt *et al.* (2018*a*) found the same scaling exponent as for the $\Gamma = 1$ case, but with a lower magnitude $f_{\text{osc}}/f_{\text{td}} \simeq 0.027Ra^{0.419}$. The scaling exponents and absolute values for measurements in larger Prandtl number fluids are generally higher. For example, in water at $Pr \sim 5.4$ scaling laws of $f_{\text{osc}} \simeq 0.2Ra^{0.46}$ (Qiu & Tong 2001), $f_{\text{osc}} \simeq 0.167Ra^{0.47}$ (Qiu *et al.* 2004), and $f_{\text{osc}} \simeq 0.12Ra^{0.49}$ (Zhou *et al.* 2009) are found.

The averaged velocity components (3.1) are also used to calculate the velocity amplitude of the LSC

$$v_{\text{LSC}} = \left\langle \frac{|\boldsymbol{v}_{\text{top}}| + |\boldsymbol{v}_{\text{bot}}|}{2} \right\rangle_t , \tag{3.3}$$

where $\langle\cdot\rangle_t$ denotes a time average. Using this velocity, the turnover time τ_{to} of the LSC can be defined as $\tau_{\text{to}} = \pi H/v_{\text{LSC}}$. Here, a roll shape in form of a circle of diameter H has been assumed as the LSC path. The turnover frequency is then

$$f_{\text{to}} = \frac{v_{\text{LSC}}}{\pi H} . \tag{3.4}$$

Figure 5(c) shows the ratio $f_{\text{osc}}/f_{\text{to}}$, which is close to unity for all Rayleigh numbers. This implies that one period of the torsional mode – and thus also of the sloshing mode – takes one turnover time of the LSC. If alternatively, the length $2H + 2L$ is used for the

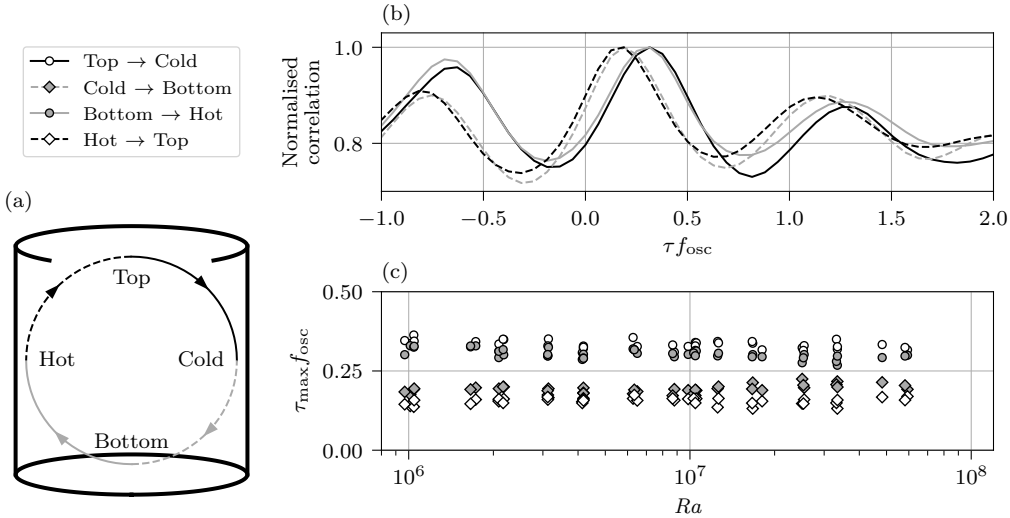

FIGURE 6. Correlation of temperature at mid height with flow orientation at the top and bottom plates. (a) Illustration of the possible correlations. (b) Example of correlations which are normalized by their maxima and plotted over the time shift τ in units of the oscillation frequency f_{osc}. The data record is taken from the measurement in figure 3 at $Ra = 6 \times 10^7$. (c) Time shift $\tau_{\max}$ of the maximal correlation over Ra.

LSC path instead of the circumference of a circle f_{to} decreases by a factor of $\pi/4 \approx 0.79$. However, the relation of $f_{\mathrm{osc}} \propto f_{\mathrm{to}}$ would still be valid.

3.3. *Interplay of the twisting and sloshing modes*

In this section, we investigate how the sloshing and torsion modes described in section 3.1 coexist and build a single coherent flow structure. The basic connection of the two modes is as follows: The flow directions at the top and bottom plate, ϕ_{top} and ϕ_{bot}, indicate the azimuthal position where the up- and down-welling flows will appear which can be monitored by the temperature sensors at mid-height. We have already shown, that on average the top and bottom flows are anti-parallel with $\langle\phi_{\mathrm{bot}}\rangle_t - \langle\phi_{\mathrm{top}}\rangle_t \sim 180°$ (see figure 3(a)). If one assumes that these flows will be deflected in different azimuthal directions by an angle $\Delta\phi$ (which stands for the effect of the LSC torsion) then the orientation angels will get closer to one another. With $\phi_{\mathrm{top/bot}} = \langle\phi_{\mathrm{top/bot}}\rangle_t \pm \Delta\phi$, the azimuthal distance of the up- and down welling flows is given by

$$\phi_{\mathrm{bot}} - \phi_{\mathrm{top}} \sim 180° - 2\Delta\phi\,. \tag{3.5}$$

With this torsion displacement $\Delta\phi$ at top and bottom getting closer to 90°, the hot up- and cold down-welling flows will also get closer to each other. This is exactly the behaviour of the sloshing mode detected in figure 3(b).

However, the flow orientation at the plates and the respective vertical flow at half-height of the cell do not coincide in time. We have established, that one oscillation period is the same as one turnover of the LSC. From this point, we would expect that the flow orientation propagates with the same speed, e.g., a given flow direction at the top plate would result in the same azimuthal position of the down-flow a quarter turnover later. To investigate this behaviour more closely, we calculate a temporal correlation of the top and bottom LSC angles with the temperatures measured at mid height (see figure 6(a)). As an example, we correlate ϕ_{top} with the down-flow at mid height, which we denote as Top → Cold. All positive values of the temperature profile are clipped in figure 3(b)

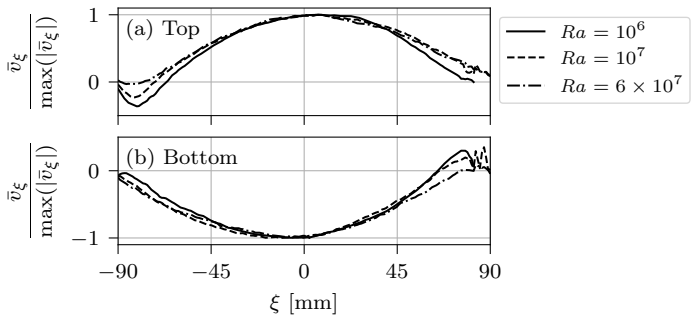

FIGURE 7. Averaged and normalized horizontal velocity profiles along the LSC at (a) the top and (b) the bottom plate for different Ra. The experiments correspond to the ones shown in figure 5(a).

to zero, in order to include the cold signature of the down-flow only. This is equivalent to clipping the temperatures to the mean fluid temperature $\bar{T}$. Next, we construct a pseudo-temperature profile $\mathcal{T}$ from the time series of ϕ_{top} which is given by

$$\mathcal{T}(\phi, t) = \begin{cases} A\cos^2\big(\phi - \phi_{\text{top}}(t)\big) & \text{for } \phi_{\text{top}} - 90^\circ < \phi < \phi_{\text{top}} + 90^\circ \\ 0 & \text{else} \end{cases} . \tag{3.6}$$

This profile emulates the temperature at mid height if the down-flow would follow the flow orientation at the top plate instantaneously. The amplitude is set to $A = -1$ in this particular case since we correlate with the negative values of the measured temperature profile. In case of a correlation with the up-welling flow, an amplitude $A = 1$ is taken. The function $\mathcal{T}$ is evaluated at the azimuthal mid-height positions of the thermocouples and correlated with the clipped temperature profile over time. The result is normalized by its maximal value and plotted in figure 6(b) as a solid black line. The correlation time shift τ is normalized by the oscillation frequency f_{osc}.

We observe that the maximum is shifted to $\tau f_{\text{osc}} > 0$, i.e., the down-flow at mid height lags behind the flow orientation at the top. The time lag of the maximum $\tau_{\max}$ is calculated by fitting a quadratic polynomial around the maximal value. In the case Top $\rightarrow$ Cold the time shift is $\tau_{\max} f_{\text{osc}} = 0.32$, which is larger than the expected value of $1/4$. The correlations of three other cases Cold $\rightarrow$ Bottom, Bottom $\rightarrow$ Hot and Hot $\rightarrow$ Top are displayed in figure 6(b) as well. It can be seen that the vertical flows at mid height have a time lag towards the flows at the respective plate, which is larger than a quarter of one oscillation period (Top $\rightarrow$ Cold and Bottom $\rightarrow$ Hot). Furthermore, the horizontal flows at the plates follow the mid-height flows with a lag shorter than a quarter oscillation period. We repeated this analysis for all our experiments. The corresponding time shifts display this behaviour (see figure 6(c)) in all data sets. On average the time lags $\tau_{\max} f_{\text{osc}}$ are: 0.33 ± 0.01 for Top $\rightarrow$ Cold, 0.19 ± 0.01 for Cold $\rightarrow$ Bottom, 0.30 ± 0.01 for Bottom $\rightarrow$ Hot, and 0.16 ± 0.01 for Hot $\rightarrow$ Top. The sum of all four time lags gives on average the expected value of one, here 0.98 ± 0.03, and thus the propagation of the flow orientation requires the same amount of time as one oscillation period or one turnover.

The deviation of the individual lags from a quarter oscillation period indicates that the LSC path is asymmetric. Such distortions might be caused by corner vortices of the LSC which are observed in simulations. We introduce here, a horizontal axis ξ that is aligned in direction of the LSC orientation. To calculate an averaged horizontal velocity profile of the LSC at the top (bottom) plate, we select the velocity profiles of the UDV sensors T_0, T_{45}, and T_{90} (B_0, B_{45}, and B_{90}) at time instants when the LSC orientation

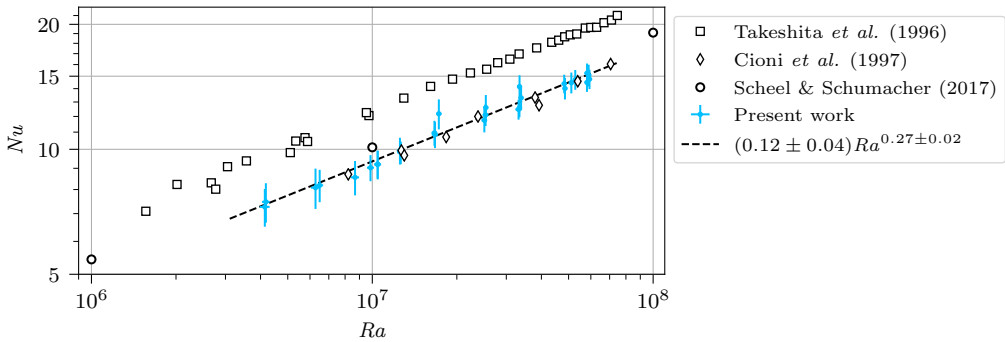

FIGURE 8. Turbulent heat transfer in the liquid metal convection flow. The scaling of Nu vs. Ra is displayed. Nu is determined from the temperature difference of the cooling water for $T_{\mathrm{out}} - T_{\mathrm{in}} > 0.2\,\mathrm{K}$. Our data are compared with a numerical simulation and two laboratory experiments, as indicated in the legend.

ϕ_{top} (ϕ_{bot}) is aligned within $\pm 5°$ with the azimuthal position of a sensor. The averages of those velocity profiles $\bar{v}_\xi(\xi)$ are normalized by their maximum magnitude and shown in figure 7 for three different Ra. It should be noted, that the noisy or missing profiles for $\xi > 80\,\mathrm{mm}$ are due to an inaccessible zone close to the UDV-sensors caused by the ringing of the piezo-crystal in the transducer. The velocities at the top plate are predominantly positive (flow to the right) and the bottom velocities are negative (flow to the left). Inverted velocities can only be seen at the positions where the up- and down-welling flows are impinging on the plates (left at the top, right at the bottom). These profiles indicate indeed the presence of recirculation vortices in the cell corners, which seem become smaller with increasing Ra. This challenges our supposition at the beginning of this paragraph that corner vortices might responsible for the different time lags in figure 6(c). With increasing Rayleigh number the fluid turbulence becomes more vigorous. This means that the vortical structures are still there, but get averaged out more effectively.

4. Turbulent transport of momentum and heat

4.1. *Heat transport*

The present section discusses the global transport properties in the liquid metal convection flow and compares the results with other experiments and simulations. We first analyse the turbulent heat transport in the experiment. The heat flux through the fluid layer is characterised by the Nusselt number Nu which is calculated at the cooled plate, $Nu = \dot{Q}_{\mathrm{cool}}/\dot{Q}_{\mathrm{cond}}$. Here, $\dot{Q}_{\mathrm{cond}} = \lambda \pi R^2 \Delta T/H$ is the purely conductive heat flux. The data is plotted over Ra in figure 8. A power law is fitted to the data using orthogonal direction regression (ODR) to incorporate the errors of both, the abscissa and the ordinate. This procedure is used for all following power law fits in this work. We find $Nu \simeq (0.12 \pm 0.04)Ra^{0.27\pm0.02}$. It agrees excellently with measurements by Cioni *et al.* (1997) in mercury ($Pr = 0.025$) and matches the numerical results by Scheel & Schumacher (2017) of $Nu \simeq (0.13 \pm 0.04)Ra^{0.27\pm0.01}$ for $Pr = 0.021$ with only a small shift. The results by Takeshita *et al.* (1996) in mercury ($Pr = 0.024$) agree with respect to the scaling exponent, but give a somewhat higher Nusselt number magnitude with $Nu \simeq 0.155Ra^{0.27\pm0.02}$.

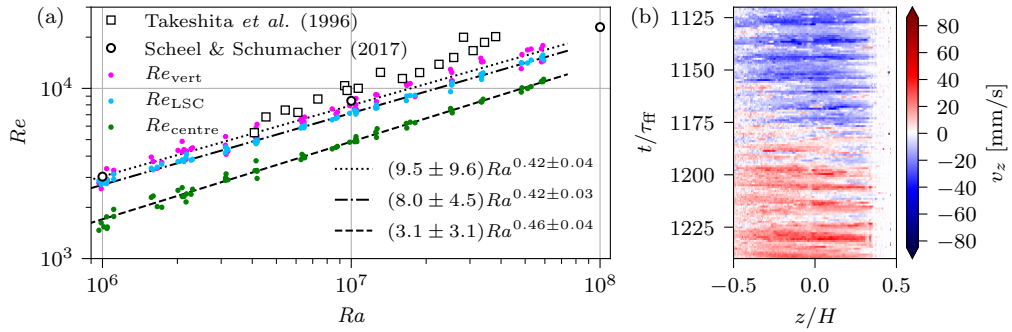

FIGURE 9. Analysis of the turbulent momentum transfer in the liquid metal convection flow based on the present UDV measurements. (a) Scaling of Reynolds number Re Rayleigh number Ra. Uncertainties of the present measurements were removed for better visibility. Their relative values are about 20 to 30 % due to the turbulent fluctuations. (b) Colour-plot of v_z measured by UDV sensor V_0 for $Ra = 6 \times 10^7$. The data correspond to the measurement shown in figure 3.

4.2. *Momentum transport*

The turbulent momentum transport of the convection flow is quantified by the Reynolds number Re. In contrast to the quantification of the turbulent heat transfer by a Nusselt number, the Reynolds number is not uniquely defined since different characteristic velocities can be employed for its definition. With the multiple probes at hand, we can define three different Re with three different corresponding characteristic velocities: 1) the typical horizontal velocity magnitude near the plates, 2) the typical vertical velocity magnitude of the LSC along the side wall and 3) the turbulent velocity fluctuations in the centre of the cell,

$$Re_{\mathrm{LSC}} = \frac{v_{\mathrm{LSC}} H}{\nu}\,, \quad Re_{\mathrm{vert}} = \frac{v_{\mathrm{vert}} H}{\nu}\,, \quad \text{and} \quad Re_{\mathrm{centre}} = \frac{v_{\mathrm{centre}} H}{\nu}\,. \tag{4.1}$$

This circumstance opens the opportunity to directly compare the sensitivity of the scaling exponent with respect to these different characteristic velocities.

First, the large scale flow is characterised by the velocity magnitude v_{LSC} as done in section 3.2. The resulting Reynolds number $Re_{\mathrm{LSC}} = v_{\mathrm{LSC}} H/\nu$ is plotted in figure 9 (blue points). A power law fit reveals a scaling of $Re_{\mathrm{LSC}} \simeq (8.0 \pm 4.4) Ra^{0.42\pm0.03}$. The exponent is close to the scaling of f_{to} and f_{osc} in figure 5(a) since $Re_{\mathrm{LSC}} = f_{\mathrm{to}} \pi H^2/\nu$.

Secondly, the vertical velocity of the LSC is measured at radial position $r/R = 0.8$ by the UDV sensor V_0. Due to the sloshing mode, the up- or down-welling flows move periodically towards and away from the sensor measuring volume. Additionally, the LSC is slowly rotating as a whole (see figure 9(b)). Since a pronounced vertical flow of the LSC is of interest only, we estimate the characteristic vertical velocity by calculating the average velocity profile $v_z(t)$ over an interval $H/4$ centered around the mid-plane for every time step, similar to (3.1). The corresponding standard deviation (std) is added to the average of the resulting velocity magnitude to accommodate for the fluctuations of this signal. Thus $v_{\mathrm{vert}} = \langle |v_z(t)| \rangle_t + \mathrm{std}(|v_z(t)|)$. This velocity gives a vertical Reynolds number $Re_{\mathrm{vert}} = v_{\mathrm{vert}} H/\nu$. The values are shown in figure 9(a) as magenta points and give a scaling of $Re_{\mathrm{vert}} \simeq (9.5 \pm 9.2) Ra^{0.42\pm0.04}$.

Finally, the turbulent velocity fluctuations are considered in the centre of the cell. Here, the three crossing UDV sensors M_0, M_{90}, and V_{c} can measure all three components of the velocity vector $\boldsymbol{v}_{\mathrm{centre}}$ (see figure 1(b)). The components are determined by taking the root-mean-square (rms) value of, again, the central $H/4$ interval of the velocity profiles.

	$Ra = 10^6$			$Ra = 10^7$			$Ra = 3.3 \times 10^7$		
$\tilde{r} = \frac{r}{R}$	$\frac{S_\xi(\tilde{r})}{S_z(\tilde{r})}$	$\frac{S_\eta(\tilde{r})}{S_z(\tilde{r})}$	$\frac{S_\eta(\tilde{r})}{S_\xi(\tilde{r})}$	$\frac{S_\xi(\tilde{r})}{S_z(\tilde{r})}$	$\frac{S_\eta(\tilde{r})}{S_z(\tilde{r})}$	$\frac{S_\eta(\tilde{r})}{S_\xi(\tilde{r})}$	$\frac{S_\xi(\tilde{r})}{S_z(\tilde{r})}$	$\frac{S_\eta(\tilde{r})}{S_z(\tilde{r})}$	$\frac{S_\eta(\tilde{r})}{S_\xi(\tilde{r})}$
0.01	1.42	0.60	0.42	1.51	0.61	0.40	1.21	0.99	0.82
0.10	1.07	0.81	0.76	0.94	0.77	0.82	0.97	0.90	0.93
0.50	1.08	1.11	1.03	1.05	0.91	0.86	1.07	0.96	0.90

TABLE 1. Comparison of second order structure functions (or second order velocity increment moment) evaluated at three distances in the centre of the convection cell for different directions. Ratios of the vertical structure function $S_z(\tilde{r})$, the horizontal structure function parallel to the LSC $S_\xi(\tilde{r})$, and the horizontal structure function perpendicular to the LSC $S_\eta(\tilde{r})$ are analysed. The table lists the ratios of the horizontal to the vertical values as well as the ratio of both horizontal function values. The data are given for three Rayleigh numbers Ra. The spatial distance r is given in units of the convection cell radius R and $\tilde{r} = r/R$.

The rms time-average of the velocity magnitude $v_{\mathrm{centre}} = \langle(\boldsymbol{v}_{\mathrm{centre}}(t))^2\rangle^{1/2}_{\mathrm{rms},t}$ is used to calculate $Re_{\mathrm{centre}} = v_{\mathrm{centre}}H/\nu$. It is plotted as green points in figure 9(a), along with the power-law fit of $Re_{\mathrm{centre}} \simeq (3.1 \pm 3.1)Ra^{0.46\pm0.04}$.

The scaling exponent of $Re_{\mathrm{centre}}(Ra)$ agrees very well with the result of DNS by Scheel & Schumacher (2017) (open circles in figure 9(a)). In the numerical simulations, the Reynolds number was calculated from the rms-velocity over the whole cell for $Pr = 0.021$ and gave a scaling of $Re \simeq (6.5 \pm 0.6)Ra^{0.45\pm0.01}$. The absolute values of Re_{centre} are about half as large as the results of the DNS, since the average over the whole cell volume also includes the high-velocity components of the LSC outside the centre region. The absolute values of Re_{LSC} and Re_{vert} match the DNS results more closely, but have a somewhat smaller exponent of 0.42.

How do our results compare to previous laboratory experiments? Measurements of a vertical Reynolds number in mercury by Takeshita *et al.* (1996) were also taken at half height and $r/R = 0.8$. They show a higher velocity magnitude with a scaling of $Re \simeq 6.24Ra^{0.46\pm0.02}$. In the $\Gamma = 2$ case, Vogt *et al.* (2018*a*) found an increased scaling exponent for a horizontal Re at the cell centre: $Re \simeq 5.662Ra^{0.483}$. Comparing all these results underlines the dependence of the momentum transport on the specific velocity that enters the Reynolds number definition. The somewhat smaller scaling exponent for the horizontal and vertical LSC velocities in comparison to previous experiments or the DNS can thus be considered as a result of probing different parts of the complex three-dimensional flow structure that we analysed before, as well as using different measurement techniques and procedures of calculating the characteristic velocities. Interestingly, the turbulent fluctuations seem to be the best indication of the global momentum transport scaling as reported by DNS, albeit being smaller in their absolute magnitude.

5. Small-scale flow structure in the center of the convection cell

The UDV measurements in liquid metal convection monitor the longitudinal velocity profile along the beam line. This opens the possibility to analyse the statistics of longitudinal velocity increments and thus the small-scale statistics in the bulk. We consider longitudinal velocity increments which are given by $\delta_r v(t) = [\boldsymbol{v}(\boldsymbol{x} + \boldsymbol{r}, t) - \boldsymbol{v}(\boldsymbol{x}, t)] \cdot \mathbf{r}/r$. The velocity profiles v are measured by the UDV sensors M_0, M_{90}, and V_{c}.

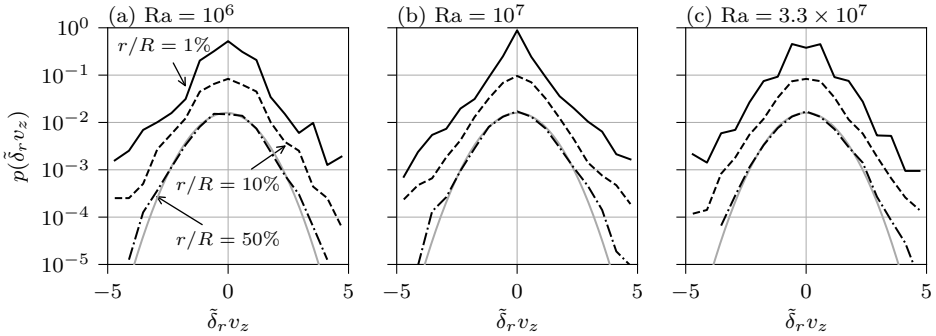

FIGURE 10. Probability density functions (PDF) of the normalized velocity increments $\tilde{\delta}_r v_z$, calculated from the UDV sensor V_c. The plots (a) to (c) show different Rayleigh numbers. The styles of the black lines correspond to the spatial increment r as specified in (a). The PDF for higher r are successively shifted by a factor of 0.2 for a better visibility. The grey line is a normal distribution with mean and variance of the PDF for $r/R = 50\%$.

Vertical velocity profiles $v_z(z,t)$ are taken directly from the UDV sensor V_c. Horizontal velocity profiles, however, have to be considered in their relation to the LSC orientation. In line with the discussion in section 3.3, we collect the velocity profiles $v_\xi(\xi,t)$ of the UDV sensors M_0 and M_{90} when the mean LSC orientation angle ϕ_{LSC} is aligned within $\pm 5°$ with the beam line of these sensors. Additionally, we introduce a horizontal axis η, which is perpendicular to the LSC orientation and collect the horizontal velocity profiles $v_\eta(\eta,t)$ from M_0 and M_{90} when $\phi_{\mathrm{LSC}} + 90°$ is aligned with the sensors. The analysis is thus conditioned to the LSC orientation.

In order to quantify the degree of isotropy of the velocity fluctuations in the turbulent flow, we start with a comparison of the longitudinal second order structure functions or velocity increment moments which are given by

$$S_i(r_i) = \langle (\delta_r v_i)^2 \rangle_{\boldsymbol{x},t} \,, \tag{5.1}$$

where $i = \xi, \eta, z$. The average is taken with respect to time and to point along the beam line. Table 1 shows the mutual ratios of these moments for three distances $\tilde{r} = r/R$ with R being the cell radius. Approximate isotropy would follow when these ratios are very close to unity. Our data clearly indicate that this is not the case, particularly for the smallest separation. The data suggest that the LSC flow is responsible for these deviations and affects the fluctuations over a wide range of scales. The present Rayleigh numbers are small in comparison to the measurements by Mashiko *et al.* (2004) at $Pr = 0.024$ or the direct numerical simulations by Kunnen *et al.* (2008) at $Pr = 4$ such that we cannot present a scaling analysis of the second order structure function.

Figure 10 shows the probability density functions (PDF) of the normalized vertical velocity increment $\tilde{\delta}_r v_z = \delta_r v_z / (\delta_r v_z)_{\mathrm{rms}}$ for the same separations $\tilde{r}$ and Rayleigh numbers Ra as in table 1. We have verified that the quantitative behavior of the corresponding PDFs of $\tilde{\delta}_\xi v_\xi$ and $\tilde{\delta}_\eta v_\eta$ is the same (and thus not displayed). For all values of Ra the PDF approaches a normal distribution with increasing increment size, a result which is well-known from homogeneous isotropic turbulence (see e.g. the DNS by Gotoh *et al.* (2002)). For the smallest separation the PDF is characterized by exponential tails. Even though, we were not able to resolve far tails of the PDFs, which are stretched exponential, our distributions reflect an intermittent, fully developed fluid turbulence in the bulk of the cell.

6. Conclusion

We presented an analysis of turbulent liquid metal convection in a cylindrical cell with aspect ratio $\Gamma = 1$. The combination of multiple UDV and temperature measurements allowed us to reconstruct and characterize essential features of the 3D large-scale circulation in the cell experimentally. The dynamics of the LSC is a superposition of different dynamical processes on different time scales. The slow meandering of the large-scale flow orientation in the closed cell proceeds at a scale of the order of about 10^3 free-fall time units in the present parameter range – a time scale that is not accessible in DNS at such low Prandtl numbers. The torsional and sloshing modes of the LSC, which are known from studies in water, could be detected by velocity and temperature measurements in the present low-Pr experiment. We find a very synchronous sloshing at a time scale of $10\tau_{\mathrm{ff}}$ that suggests a more coherent large-scale flow as for higher Pr. This time scale is consistent with temperature measurements of older experiments in mercury and recent DNS. It also coincides with the turnover time of the LSC. The temporal correlations between different segments of the LSC, which we verified by combination of velocity and temperature measurements are nearly independent of the Rayleigh number. Cessations of the large-scale flow remain rare events in the low-Prandtl-number convection regime. In summary, our analysis supports the picture a very coherent large-scale flow in the closed cell for turbulent convection at such low Prandtl number.

The turbulent momentum transport was determined in multiple ways in the cell by *direct* velocity measurements. Depending on the UDV beam line position with respect to the large-scale flow, the resulting Re can vary by a factor of two or even more in amplitude. The scaling behaviour with respect to the Rayleigh number is found to agree well with previous studies. The same holds for the turbulent heat transfer. The present ultrasound measurements of velocity increments reveal an inertial fluid turbulence in the bulk, e.g., by extended tails of the distribution of small-separation increments. We also showed that coherent large-scale flow seems to prevent the establishment of local isotropy in the bulk, a point that might be worth to be deeper explored in simulations.

Our study is based to a large part on direct velocity field measurements in the liquid metal flow. Even though several of the properties that we discussed are known from convective turbulence in air or water, one value of this work is to demonstrate these features in an opaque liquid metal flow. This circumstance becomes even more once these experiments are pushed to higher Rayleigh numbers in GaInSn or to even lower Prandtl numbers such as liquid sodium. In those parameter ranges the total integration times in direct numerical simulations will be even shorter and experiments are the only way to study longer-term evolutions in the convection flow.

TZ and FS are supported by the Deutsche Forschungsgemeinschaft with Grants No. GRK 1567 and No. VO 2332/1-1, respectively. We thank Janet D. Scheel and Christian Resagk for useful comments and discussions.

REFERENCES

Adrian, R. J. & Westerweel, J. 2011 *Particle Image Velocimetry*. Cambridge University Press.

Ahlers, G., Grossmann, S. & Lohse, D. 2009 Heat transfer and large scale dynamics in turbulent Rayleigh-Bénard convection. *Rev. Mod. Phys.* **81** (2), 503–537.

Brown, E. & Ahlers, G. 2006 Rotations and cessations of the large-scale circulation in turbulent Rayleigh–Bénard convection. *J. Fluid Mech.* **568**, 351–386.

Brown, E. & Ahlers, G. 2009 The origin of oscillations of the large-scale circulation of turbulent Rayleigh–Bénard convection. *J. Fluid Mech.* **638**, 383–400.

Chillà, F. & Schumacher, J. 2012 New perspectives in turbulent Rayleigh-Bénard convection. *Eur. Phys. J. E.* **35** (7), 58.

Christensen, U. R. & Aubert, J. 2006 Scaling properties of convection-driven dynamos in rotating spherical shells and application to planetary magnetic fields. *Geophys. J. Int.* **166** (1), 97–114.

Cioni, S., Ciliberto, S. & Sommeria, J. 1997 Strongly turbulent Rayleigh–Bénard convection in mercury: Comparison with results at moderate Prandtl number. *J. Fluid Mech.* **335**, 111–140.

Franke, S., Lieske, H., Fischer, A., Büttner, L., Czarske, J. W., Räbiger, D. & Eckert, S. 2013 Two-dimensional ultrasound Doppler velocimeter for flow mapping of unsteady liquid metal flows. *Ultrasonics* **53** (3), 691–700.

Funfschilling, D. & Ahlers, G. 2004 Plume Motion and Large-Scale Circulation in a Cylindrical Rayleigh-Bénard Cell. *Phys. Rev. Lett.* **92** (19), 194502.

Gotoh, T., Fukayama, D. & Nakano, T. 2002 Velocity field statistics in homogeneous steady turbulence obtained using a high-resolution direct numerical simulation. *Phys. Fluids* **14**, 1065–1081.

Hoyer, K., Holzner, M., Lüthi, B., Guala, M., Liberzon, A. & Kinzelbach, W. 2005 3D scanning particle tracking velocimetry. *Exp. Fluids* **39** (5), 923–934.

Kelley, D. H. & Weier, T. 2018 Fluid Mechanics of Liquid Metal Batteries. *Appl. Mech. Rev.* **70** (2), 020801.

Khalilov, R., Kolesnichenko, I., Pavlinov, A., Mamykin, A., Shestakov, A. & Frick, P. 2018 Thermal convection of liquid sodium in inclined cylinders. *Phys. Rev. Fluids* **3** (4), 043503.

Kunnen, R. P. J., Clercx, H. J. H., Geurts, B. J., van Bokhoven, L. J. A., Akkermans, R. A. D. & Verzicco, R. 2008 Numerical and experimental investigation of structure-function scaling in turbulent Rayleigh-Bénard convection. *Phys. Rev. E* **77**, 016302.

Mashiko, T., Tsuji, Y., Mizuno, T. & Sano, M. 2004 Instantaneous measurement of velocity fields in developed thermal turbulence in mercury. *Phys. Rev. E* **69** (3), 036306.

Müller, U. & Bühler, L. 2001 *Magnetofluiddynamics in Channels and Containers*. Berlin: Springer Verlag.

Plevachuk, Y., Sklyarchuk, V., Eckert, S., Gerbeth, G. & Novakovic, R. 2014 Thermophysical Properties of the Liquid Ga–In–Sn Eutectic Alloy. *J. Chem. Eng. Data* **59** (3), 757–763.

Qiu, X.-L., Shang, X.-D., Tong, P. & Xia, K.-Q. 2004 Velocity oscillations in turbulent Rayleigh–Bénard convection. *Phys. Fluids* **16** (2), 412–423.

Qiu, X.-L. & Tong, P. 2001 Onset of Coherent Oscillations in Turbulent Rayleigh-Bénard Convection. *Phys. Rev. Lett.* **87** (9), 094501.

Salavy, J.-F., Boccaccini, L. V., Lässer, R. L., Meyder, R., Neuberger, H., Poitevin, Y., Rampal, G., Rigal, E., Zmitko, M. & Aiello, A. 2007 Overview of the last progresses for the European Test Blanket Modules projects. *Fusion Eng. Des.* **82** (15), 2105–2112.

Scheel, J. D. & Schumacher, J. 2016 Global and local statistics in turbulent convection at low Prandtl numbers. *J. Fluid Mech.* **802**, 147–173.

Scheel, J. D. & Schumacher, J. 2017 Predicting transition ranges to fully turbulent viscous boundary layers in low Prandtl number convection flows. *Phys. Rev. Fluids* **2** (12), 123501.

Schumacher, J., Bandaru, V., Pandey, A. & Scheel, J. D. 2016 Transitional boundary layers in low-Prandtl-number convection. *Phys. Rev. Fluids* **1** (8), 084402.

Shi, N., Emran, M. S. & Schumacher, J. 2012 Boundary layer structure in turbulent Rayleigh–Bénard convection. *J. Fluid Mech.* **706**, 5–33.

Spiegel, E. A. 1962 Thermal Turbulence at Very Small Prandtl Number. *J. Geophys. Res.* **67** (8), 3063–3070.

Stevens, R. J. A. M., Clercx, H. J. H. & Lohse, D. 2011 Effect of plumes on measuring the large scale circulation in turbulent Rayleigh-Bénard convection. *Phys. Fluids* **23** (9), 095110.

Sun, C., Xia, K.-Q. & Tong, P. 2005 Three-dimensional flow structures and dynamics of turbulent thermal convection in a cylindrical cell. *Phys. Rev. E* **72** (2), 026302.

Takeda, Y. 1987 Measurement of Velocity Profile of Mercury Flow by Ultrasound Doppler Shift Method. *Nucl. Technol.* **79** (1), 120–124.

Takeshita, T., Segawa, T., Glazier, J. A. & Sano, M. 1996 Thermal turbulence in mercury. *Phys. Rev. Lett.* **76** (9), 1465.

Toschi, F. & Bodenschatz, E. 2009 Lagrangian Properties of Particles in Turbulence. *Annu. Rev. Fluid Mech.* **41** (1), 375–404.

Tsuji, Y., Mizuno, T., Mashiko, T. & Sano, M. 2005 Mean Wind in Convective Turbulence of Mercury. *Phys. Rev. Lett.* **94** (3), 034501.

van der Poel, E. P., Stevens, R. J. A. M. & Lohse, D. 2013 Comparison between two- and three-dimensional Rayleigh–Bénard convection. *J. Fluid Mech.* **736**, 177–194.

Vogt, T., Horn, S., Grannan, A. M. & Aurnou, J. M. 2018*a* Jump Rope Vortex in Liquid Metal Convection. *Proc. Natl. Acad. Sci. USA* **115** (50), 12674–12679.

Vogt, T., Ishimi, W., Yanagisawa, T., Tasaka, Y., Sakuraba, A. & Eckert, S. 2018*b* Transition between quasi-two-dimensional and three-dimensional Rayleigh-Bénard convection in a horizontal magnetic field. *Phys. Rev. Fluids* **3** (1), 013503.

Xi, H.-D., Zhou, S.-Q., Zhou, Q., Chan, T.-S. & Xia, K.-Q. 2009 Origin of the Temperature Oscillation in Turbulent Thermal Convection. *Phys. Rev. Lett.* **102** (4), 044503.

Xie, Y.-C., Wei, P. & Xia, K.-Q. 2013 Dynamics of the large-scale circulation in high-Prandtl-number turbulent thermal convection. *J. Fluid Mech.* **717**, 322–346.

Zhou, Q., Xi, H.-D., Zhou, S.-Q., Sun, C. & Xia, K.-Q. 2009 Oscillations of the large-scale circulation in turbulent Rayleigh–Bénard convection: The sloshing mode and its relationship with the torsional mode. *J. Fluid Mech.* **630**, 367–390.